TRANSACTIONS ON ELECTRICAL ENGINEERING

CONTENTS

Vol. 8 (2019) **No. 2** **pp. 17 – 31**

ERGO NOMEN

TRANSACTIONS ON ELECTRICAL ENGINEERING

Publisher: ERGO NOMEN, o.p.s., K13114 FEE CTU in Prague,
Technicka 1902/2, 166 27 Praha 6, Czech Republic
E-mail: info@transoneleng.org

Periodicity: Quarterly
Language: English
Scope: International scientific journal of electrical engineering
On-line version: www.transoneleng.org
ISSN 1805-3386

Each paper in the journal is evaluated by two reviewers under the supervision of the International Editorial Board.

Responsibility for the contents of all the published papers and technical notes is upon the authors. Template in MS WORD and basic typographic rules to be followed see www.transoneleng.org.

Development of Urban Electric Bus Drivetrain

Oleg Sivkov [1)], Lubomir Musalek [2)], Jaroslav Novak [3)], Martin Novak [4)] Jan Chysky [5)], and Lukas Novak [6)]

[1)] Czech Technical University in Prague, Faculty of Mechanical Engineering, Prague, Czech Republic, e-mail: *oleg.sivkov@fs.cvut.cz*

[2)] Czech Technical University in Prague, Faculty of Mechanical Engineering, Prague, Czech Republic, e-mail: *lubomir.musalek@fs.cvut.cz*

[3)] Czech Technical University in Prague, Faculty of Mechanical Engineering, Prague, Czech Republic, e-mail: *jaroslav.novak@fs.cvut.cz*

[4)] Czech Technical University in Prague, Faculty of Mechanical Engineering, Prague, Czech Republic, e-mail: *martin.novak@fs.cvut.cz*

[5)] Czech Technical University in Prague, Faculty of Mechanical Engineering, Prague, Czech Republic, e-mail: *jan.chysky@fs.cvut.cz*

[6)] Czech Technical University in Prague, Faculty of Mechanical Engineering, Prague, Czech Republic, e-mail: *lukas.novak@fs.cvut.cz*

Abstract — **The development of the drivetrain for a new series of urban electric buses is presented in the paper. The traction and design properties of several drive variants are compared. The efficiency of the drive was tested using simulation calculations of the vehicle rides based on data from real bus lines in Prague. The results of the design work and simulation calculations are presented in the paper.**

Keywords — Electric Bus; traction battery; simulation calculation; drive concept.

I. Introduction

The main goals of the project can be summarized as follows:

1. Proposal of a new concept for a drivetrain with increased efficiency.
2. Specify the main parameters of the drivetrain components.
3. Verification through simulation and optimization of the parameters for the drivetrain components (simulation of vehicle driving in real routes, evaluation of traction and energy parameters).
4. Specify battery cell parameters.
5. Verify experimentally the properties of considered battery cells and the measurement results in the use of simulation calculations.
6. Proposal of the electromechanical converter design.
7. Proposal regarding the construction and control of the converter part.
8. Proposal regarding the construction of battery equipment and battery management system.
9. Implement the drive unit and the converter equipment.
10. Perform laboratory tests of the drive unit and converter equipment.
11. Install the drive system, converter equipment, and battery on the vehicle.
12. Realize commissioning of the drive system.
13. Conduct extensive testing and evaluation of the system.

The Faculty of Mechanical Engineering of CTU in Prague is mainly involved in activities 1 to 5, 10 and 13 of the mentioned above points. At present, the activities in points 1, 2, 3 are currently being processed. An experimental background for testing battery cells according to point 5 has been implemented.

II. Electrobus Power Supply Structure

The structure of the electric bus drivetrain is relatively simple and standard. The input DC circuit of the traction inverter is supplied from the rechargeable battery via a bidirectional DC / DC converter which supplies the three-phase motor. There is a system of mechanical energy transfer to the axle.

The DC / DC converter is used to adjust the voltage levels of the battery and the input of the traction inverter. At the same time, it stabilizes the input voltage of the inverter and eliminates battery voltage fluctuations due to its discharge and voltage drop at the internal resistance.

The traction inverter has a standard connection; it is a three-phase bridge with six IGBTs and six flyback diodes. The traction inverter forms an output three-phase system using pulse width modulation (PWM).

The innovation compared to current SOR electric buses, which are equipped with traction induction motors, is the vision to use a permanent magnet synchronous motor (PMSM). Using a PMSM can be characterized in the following points:

- Smaller dimensions and weight compared to induction motor.
- Larger torque overload than an induction motor (up to 3×).
- Instantaneous response for the transition to electrodynamics' brake due to permanent magnet excitation.
- The necessity of solution of motor disconnection in case of traction circuit faults (magnetic flux is permanent in motor).

A dominant feature of PMSM compared to induction motors is the reduction of dimensions and weight. Several differences are compared to the asynchronous motor, also

TELEN2019010
DOI 10.14311/TEE.2019.2.017

in the solution of the torque control structure and the necessity of using the rotor angle sensor. This issue was previously addressed in [6].

A conceptual issue that has not yet been resolved is the concept of transferring mechanical energy from the electric motor shaft to the axle. An axle gearbox is used in each case. Further, the structure of mechanical transmission may be processed via two options:

1. Transmission from the motor shaft directly to the input axle transmissions.
2. Inserting a shiftable gearbox between the engine and axle transmission.

In the case of a shiftable gearbox, two gear reductions are considered. The first gear reduction with the transfer gear embedded 1.8 and the second gear reduction where the torque is transmitted from the engine directly to the input axle transmission i.e. with the first gear. The insertion of a shiftable gearbox complicates the design and deteriorates driving characteristics, especially the pulling and braking forces of the gear shift. On the other hand, using a shiftable gearbox provides background for smaller dimensions and weight of the motor to achieve a higher climbing rate and use of a lower voltage. Support for the decision on the final version is obtained by simulation calculations of the vehicle on specific routes.

III. Specification of Main Drive Parameters

When designing the main drive and motor parameters, it is necessary to take into account the main requirements of the vehicle and other limiting requirements given by the design of both mechanical and electrical parts. For a quick calculation of basic parameters, especially for the electric motor, the calculation of parameters in the MS EXCEL was prepared at CTU Faculty of Mechanical Engineering. The calculation assume the use of a permanent magnet synchronous motor (PMSM). The following values are entered as input variables:

- Limit voltage U_{max}, which is limited primarily by the voltage level of the power semiconductor components of the traction converter. The maximum voltage is limited to 1000 V for safety reasons and mainly for reasons of legislation, so that people trained for low voltage could work on that equipment.
- Total mechanical gear reduction ratio i_{total} is specified as the product of individual gearbox gear ratio.
- The total efficiency of the transmission η_{total} is the product of both gearboxes efficiency.
- Wheel radius r_w.
- Maximum vehicle speed v_{max}.
- The relative speed of the motor to field weakening related to the maximum motor speed $n_{Fluxweakening}$.
- The relative voltage drop across R and L on motor impedance ΔU_{RLrel} at a nominal speed of the motor.
- Weight of the vehicle m_v.
- Climbing rate of the vehicle in %.
- Vehicle acceleration at maximum climb.
- The sum of the driving resistances of vehicle F_{dr} in addition to the resistance from acceleration and resistance from the climb (air resistance, rolling resistance, resistances in vehicle components) – is given as constant, approximate, value and applies approximately to start and for low speed.
- Rotational mass coefficient ξ.
- Motor overload capacity p_M as the ratio of maximum and nominal torque.
- Motor efficiency η_M – estimate.
- Motor power factor $\cos\varphi_n$ – estimate.
- Maximum and minimum cell voltage battery $U_{cellmax}$ and $U_{cellmin}$.
- Maximum battery voltage U_{batmax}.
- Inverter efficiency η_{Inv} – estimate.

The calculation is based on the definition of the motor nominal values (voltage, current, torque) with which the motor can be operated indefinitely and on the overload limit values where it can operate for a limited time. If the motor is running in overload, the operation time is dependent on the amount of instantaneous overload. Due to the vector control torque motor structure, the equality of torque and current overload is assumed in the calculation. This equality applies exactly when flux weakening is not used. In flux weakening this equality is approximate. With the increasing speed at constant current overload, the torque overload decreases.

The calculation procedure is discussed in literature [1], [7]. Based on calculations 18 options of electric motors and gearboxes parameters were determined, and from these ten options, two priority options were selected. One with shiftable gearbox, the other with fixed torque transmission from motor to the axle gearbox input. The options can be characterized by the following main parameters:

Fixed gear variant:	
Nominal motor power	161 kW
Vehicle climb rate	20 %
Vehicle weight	19.4 t
Voltage limit	750 V
Maximum vehicle speed	80 km/h
Total gear ratio (on axle)	7.36
Acceleration at maximum climb	0.1 m/s^2
Nominal torque of motor	917 Nm
Nominal speed of motor	1683 rpm
Maximum speed of motor	3367 rpm
Nominal voltage of motor	392 V
Nominal current of motor	251 A
Torque and current overload	3.23

Shiftable gearbox variant:	
Nominal motor power	135 kW
Vehicle climb rate	22 %
Vehicle weight	19.4 t
Voltage limit	750 V
Maximum vehicle speed	90 km/h
Total gear ratio (axle+shiftable gearbox)	13.25
Acceleration at maximum climb	0.1 m/s^2
Nominal torque of motor	620 Nm
Nominal speed of motor	2084 rpm

TELEN2019010
DOI 10.14311/TEE.2019.2.017

Maximum speed of motor	3789 rpm
Nominal voltage of motor	324 V
Nominal current of motor	281 A
Torque and current overload	3
Preferred shifting speed	50 km/h

On comparison of the two variants, the shiftable gearbox has a smaller nominal power and smaller nominal current of the motor (323 A compared to 434 A) which makes the construction of the electric equipment simpler and quicker. On the other hand, the mechanical construction is more complicated. Also, the drops in the pulling and braking force during shifting are problematic. This gear shifting takes about 0.5 s.

IV. Circuit Solution and Controlled Pulse Rectifier Function

A simulation model for the calculation of bus behavior on defined routes was prepared. It was implemented for a detailed evaluation of the traction and energy properties of the drive unit. The input parameters of the model are:

- Route parameters (stops, speeds, slopes).
- Vehicle and drive unit parameters (weight, motor parameters, gear ratios, driving resistances).

The whole calculation is based mainly on the numerical solution of the vehicle motion equation.

The efficiency map is the basis for motor losses calculation. It is determined from the motor nameplate according to [1]. For illustrative purposes, Fig. 1 shows an efficiency map for a variable speed gear motor.

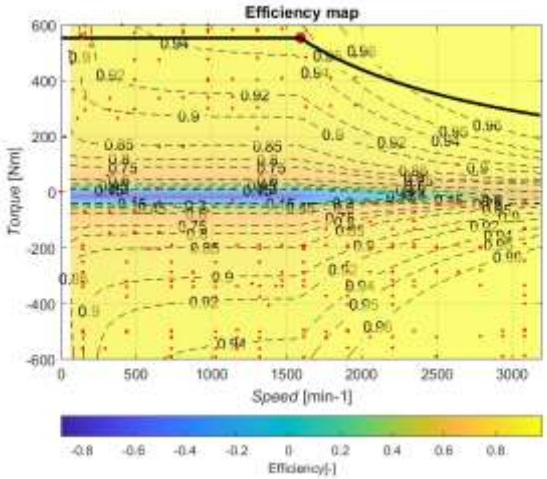

Fig. 1. Efficiency map of the motor with shiftable gearbox.

A rather complicated problem was the determination of the detailed route parameters, especially on the slope. The initial data was obtained via GPS. The route elevation was calculated from the height profile and the slope of route further from that. The route slope was determined from the height profile by parts of linear interpolation dividing into 20 linear sections. For further calculations, the route slope in a given linear section is considered to be constant. These simplifications are made in order to eliminate noise in the measured altitude data. Fig. 2 shows an example of the measured and linearized slope.

Tab. 1 illustrates examples of energy consumption calculations for two routes.

TABLE I.
Examples of Simulation Calculations – Driving with a Non-Shiftable Gearbox

Route	**Length (km)**	**Consumption (kWh) Without the slope**	**Consumption (kWh/100km) Without the slope**	**Consumption (kWh) With the slope**	**Consumption (kWh/100km) With the slope**
Cycle SORT 2	0,937	0,78	83,3	–	–
Na Knížecí –> Jinonice, line 137	4,73	2,7	57	5,8	122,6
Na Knížecí –> Jinonice, line 137, **trip 2**	4,73	2,2	46,5	5,9	124,7
Na Knížecí –> Jinonice, line 137, **trip 3**	4,73	2,7	57	5,8	122,6
Na Knížecí –> Jinonice, line 137, **trip 4**	4,73	2,2	46,5	5,9	124,7
Smíchovské nádraží –> Sídliště Zbraslav	13,2	9,2	69,7	Slope is not available	Slope is not available

TELEN2019010
DOI 10.14311/TEE.2019.2.017

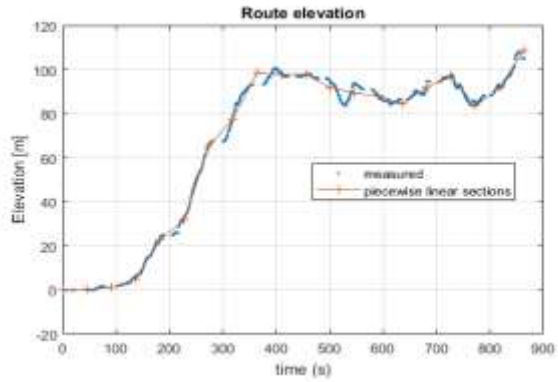

Fig. 2. Route profile – measured and linear interpolation, route "Na Knížecí" ==> "Jinonice", bus line 137.

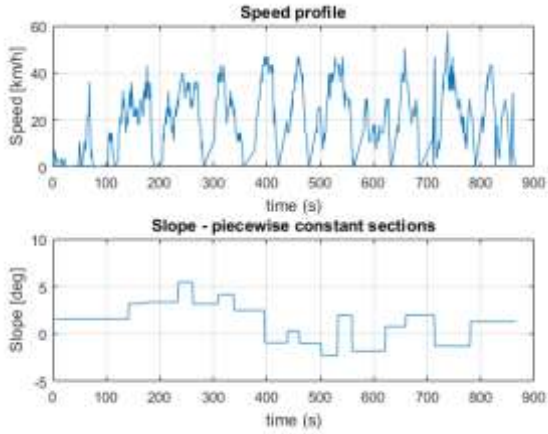

Fig. 3. Speed profile –measured and linear sections, route "Na Knížecí" ==> "Jinonice", bus line 137.

V. High Capacity Cell Testing for Traction Battery

Battery cell parameters potentially usable for traction battery of the electric bus have been tested. Three types of cells are considered – cylindrical cells NMC with capacity 2 Ah, cylindrical cells NMC with capacity 3.2 Ah and flat cells NMC with capacity 150 Ah. The testing system for 150 Ah cells which is technically more complicated will be presented here.

This section will demonstrate an innovative way of solving problems of high current source and load with constant current demand regulation. The task was to measure the charging / discharging characteristics of the 150 Ah battery Lion cell with a nominal voltage of 3.7 V. The requirement was to charge and discharge the battery with a constant current 1 A. The initial idea was to use a modified welding inverter. However, we had to leave this solution according to the problematic availability of the source for 150 Ah of continuous load. Moreover, current control for such a low voltage was uncertain with the welding source. Another possible solution was to use a 3×400 / 6 V, 600 VA transformer with a rectifier. To obtain the output DC voltage, a six-pulse two-way 3-phase block rectifier with diodes ČKD Polovodiče D200/800 was used. For current control, a frequency converter Danfoss VLT FC 302 in scalar mode was used. A feedback signal from DC / DC current converter 5000:1 LEM LT500-T is connected to the input of current converter for feedback.

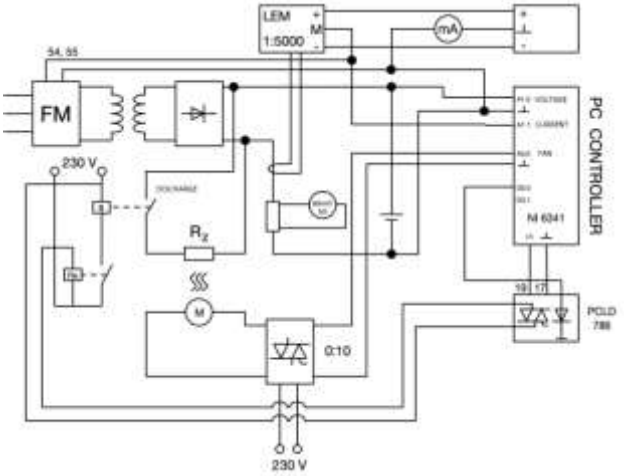

Fig. 4. Overall scheme for battery cell measurement 150 Ah.

For constant current discharge, a steel wire resistor of 2.4 mm diameter is used. The resistor value was selected to have the desired current passing through it when heated to approximately 400 °C with voltage of 4.2 V. The resistor was cooled with an axial fan. When the battery voltage is reduced, the value of current and losses on the resistor is also reduced. Thus the resistance decreases and the current increases. For precise adjusting of the discharge current, the controller regulates the fan speed and thus the load resistor cooling and its resistance.

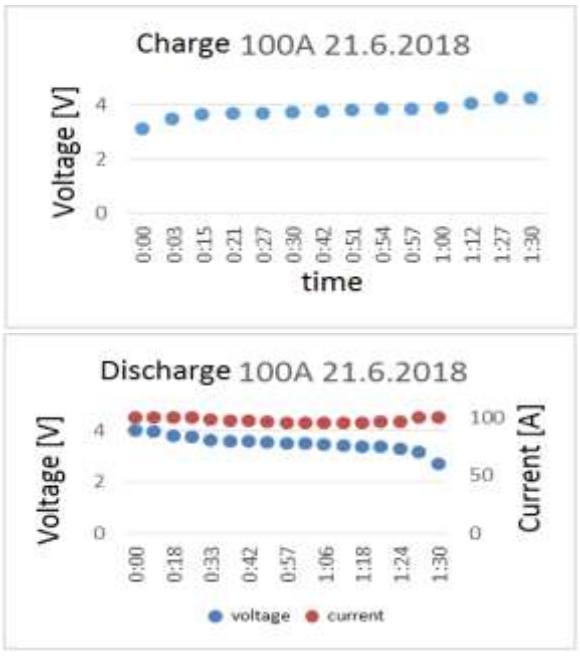

Fig. 5. Recorded charging and discharging process of the cell.

The possibility of non-conventional use of frequency converter as a control unit for a current source for battery charging and at the same time the possibility of regulating the discharge current by changing the temperature of the load resistor has been experimentally demonstrated.

VI. Conclusion

The considered variants are a drivetrain with the shiftable gearbox but with shifting minimization or with no shifting and driving with a permanently engaged gear 1 (urban traffic) or 2 (intercity traffic in the flat section of

TELEN2019010
DOI 10.14311/TEE.2019.2.017

track). At the same time, the specification of the rechargeable battery is prepared on the basis of energy simulation calculations.

ACKNOWLEDGMENT

This paper was supported by the project from the Czech Ministry of Industry and Trade, TRIO FV 30213 Research and development of traction system of an electric bus with higher efficiency.

Within the MPO TRIO program, a project focused on the development of a new drive system for the SOR electric bus was supported. The project investigators are the companies: SOR, Rail electronics (supplier of inverter equipment and control systems) and CTU in Prague, Faculty of Mechanical Engineering, Department of Instrumentation and Control Engineering.

REFERENCES

[1] J. Novák, M. Novák, Z. Novák, and J. Chyský, "Calculation and Experimental Investigation of Efficiency Map of Electric Motor" (in Czech: "Výpočet a experimentální vyšetřování účinnostní mapy elektromotoru"), in *Proceedings of XXXV. Electric Drive Conference 2017*, University of West Bohemia in Pilsen, 2017, ISBN 978-80-02-02724-9.

[2] J. Novák, O. Sadílek, and P. Sýkora, "Lithium Traction Accumulators for Electromobility" (in Czech: "Lithiové trakční akumulátory pro elektromobilitu"), Part 2, *ELEKTRO 2016*, Vol. 26, No. 11 and 12, published by FCC Public, Prague 2016, ISSN 0322-9025.

[3] SOR company materials

[4] Materials of the company Railelectronics

[5] VUES company materials

[6] J. Novák, *Torque Control Structure for Traction Synchronous Motor with Permanent Magnets* (in Czech: Regulační struktura momentu pro trakční synchronní motor s permanentními magnety), Technical Report for Railelectronics, CTU in Prague, Faculty of Mechanical Engineering, Prague, 2013.

[7] J. Novák and M. Novák, *Selected Problems of Electrical Bus Electric Drive Design* (in Czech: Vybrané problémy návrhu elektrického pohonu elektrobusu), Technical Report, CTU in Prague, Faculty of Mechanical Engineering, 2018.

[8] Danfoss company materials

Oleg Sivkov got the MSc. degree in Electric engineering in 2002 from the Faculty of Electrical Engineering at South Ural State University in Chelyabinsk. In 2011 he has received a PhD degree from the Department of Electric Drives and Traction, Faculty of Electrical Engineering at Czech Technical University in Prague. He works as an assistant professor since 2013 at the Department of Instrumentation and Control Engineering, Faculty of Mechanical Engineering at Czech Technical University in Prague. He currently works with research in the field of controlling the permanent magnet synchronous motor. E-mail: oleg.sivkov@fs.cvut.cz

Lubomír Musálek graduated the specialization of Electric Power Engineering at Electric Engineering Faculty of CTU in Prague in 2011. He works at Faculty of Electric Engineering at Czech Technical University in Prague as an assistant professor. He is specialized in electrical power engineering. E-mail: lubomir.musalek@fs.cvut.cz

Jaroslav Novák received the MSc. degree in Power Electronics in 1989 from the Faculty of Electrical Engineering at the Czech Technical University in Prague, Czech Republic. In the year 1992 he has received a CSc. degree (Ph.D.) from the Department of Electrical Drives and Traction on the same faculty. He was working since 1992 as an assistant professor, since 2003 as an associated professor on the Department of Instrumentation and Control Engineering on the Faculty of Mechanical Engineering, CTU in Prague. Since 2011 he works as a professor at Transportation Faculty of Jan Perner of Pardubice University and continues cooperating with Mechanical Engineering Faculty of CTU in Prague. His main field of interest is electric drives, power electronics, electric traction, and microprocessor control.
E-mail: jaroslav.novak@fs.cvut.cz

Jan Chyský is an associate professor graduated from the specialization Technical Cybernetics at Czech Technical University in Prague. After graduation, from 1979 he works at Faculty of Mechanical Engineering, gradually at the Departments of Automation and Electrical Engineering. In 1992 he was appointed an associate professor in the Electrical Engineering Division at Mechanical Engineering Faculty. From 2009 to 2019 he was the head of the Department of Instrumentation and Control Engineering. His professional activities are focused on the application of embedded systems for modeling, diagnostics and management of production facilities with a focus on reducing energy intensity and improving environmental parameters.
E-mail: jan.chysky@fs.cvut.cz

Martin Novák received the MSc. degree in Instrumentation and Control Engineering in 2003 from the Faculty of Mechanical Engineering at the Czech Technical University in Prague, Czech Republic. He continued with a PhD. degree (2008) at the same university. In 2013 he was appointed an associate professor. His main areas of interest are microcontrollers, signal processing, measuring methods and instruments, power electronics and control systems of permanent magnet synchronous machines.
E-mail: martin.novak@fs.cvut.cz

Lukáš Novák graduated the specialization of Electric Machines and Drives at Electric Engineering Faculty of CTU in Prague in 1984. He defended his doctoral thesis on Non-Disassembly Diagnostics of Combustion Engines in 2004. He works at Faculty of Electric Engineering at Czech Technical University in Prague as an associate professor. He is specialized in the automation of production machines and their drives.
E-mail: lukas.novak@fs.cvut.cz

TELEN2019010
DOI 10.14311/TEE.2019.2.017

High Performance IIR Filter FPGA Implementation Utilizing SOS Microcode Core

Ing. Ondřej Zoubek, Ph.D.[1)] and Ing. Tomáš Musil, Ph.D.[2)]
[1)] FEE CTU in Prague, Prague, Czech Republic, e-mail: *zoubeon1@fel.cvut.cz*
[2)] FTS CTU in Prague, Prague, Czech Republic, e-mail: *musil@fd.cvut.cz*

Abstract — **This paper discusses the methods of optimal IIR filter FPGA implementation. The methods are focused on the reduction of occupied resources and increasing data throughput. Higher demands on an internal controller complexity are successfully solved by utilizing programmable microcode controller. The novelty of SOS core and its capabilities are presented and different variants of SOS core are assessed. The workflow of IIR filter design using MATLAB considering rounded coefficient method is demonstrated.**

Keywords — digital filters, FPGA, high throughput, IIR filter, microcode, MSOSps, Second Order Section.

I. Introduction

The Infinite Impulse Response (IIR) digital filter design is well known for decades and a great variety of Field Programmable Gate Array (FPGA) and CMOS process implementations have been published. Nevertheless, the performance of published IIR filter [1], [2] implementations in proportion to occupied FPGA fabric resources do not reach optimal levels. This is particularly important for mid-range FPGAs where a non-optimal design of a simple IIR filter can easily deplete FPGA resources. One of the ways how to reduce the logic complexity and resources demands to implement an IIR filter is to fit arithmetical resources optimally to requirements of the given signal. Time sharing of the FPGA most valuable resources is the other way how to reach higher performance. Dividing of complex IIR filters into 2nd Order Sections (SOS) helps in both cases [3], [4].

II. SOS Computation Complexity

Referring to Fig. 1 it can be seen that for implementing of 2nd order IIR filter it is necessary to multiply with four different constants (b_1, b_2, a_1, a_2) and add five values ($x(n)$, $x(n-1)\cdot b_1$, $x(n-2)\cdot b_2$, $y(n-1)\cdot a_1$, $y(n-2)\cdot a_2$) and accumulate them.

The values used for computation are filter input values $x(n)$, $x(n-1)$, $x(n-2)$ and filter output values $y(n-1)$ and $y(n-2)$. The output value $y(n)$ have to be saved for next computation.

Assuming that the filter input value $x(n)$ must be also stored somewhere, the whole 2nd order IIR digital filter requires six memory elements (word bit width according to requested arithmetical accuracy).

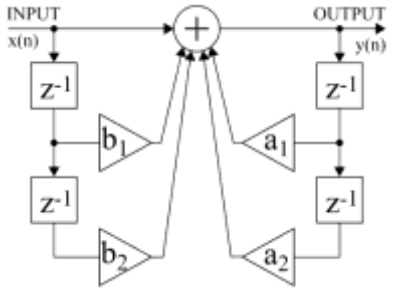

Fig. 1. General 2nd order IIR digital filter.

Mentioned general 2nd order IIR digital filter can be considered as a basic building SOS block of all other more complex IIR filters.

According to conventional design methods and fabric resources of mid-range FPGA (Spartan-6 family by Xilinx Inc. can be considered as an example of mid-range FPGA) one SOS consuming 4 multipliers and 4 adders in case of using recursion. That means 144 D-type flip-flops in rather common 24 bit arithmetic, not mentioning pipeline registers at this place. The computing of one value would take one system clock, specifically on Spartan-6, computing frequency can exceed 100 MHz, although this design speed is not necessary for many applications. On the other side, designs with more 2nd Order Sections for implementation of higher order IIR filters or more individual digital filters imply structure replication and spending multiple resources.

In applications where filter sample frequency versus design frequency ratio allows it the adders and the multipliers can be time multiplexed (see Fig. 2) and the memory places can be shared between 2nd Order Sections (see Fig. 3). For the purpose of researching, the amount of resources used for computation of one 2nd Order Section MSOSps (Mega SOS per second) was defined. One multiplier and one adder in mid-range FPGA possibly carry out 12.5 to 20 MSOSps at 100MHz frequency according to pipeline length and controller complexity. For higher MSOSps performance utilizing of more adders and multipliers is necessary.

TELEN2019008
DOI 10.14311/TEE.2019.2.022

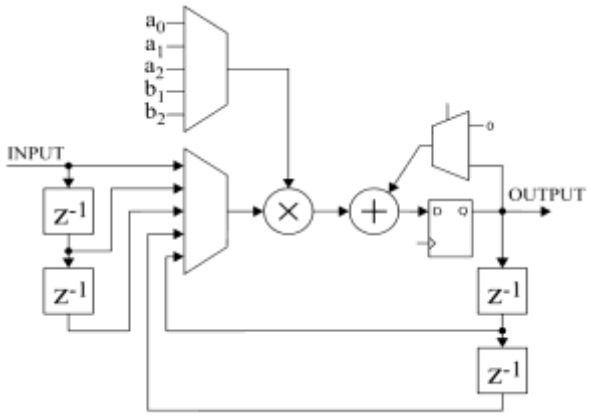

Fig. 2: Time multiplexed computation of SOS.

If the computation is processed in time multiplex with the adder (the accumulator) the length of accumulation determines the ratio between the amount of data stored and data fetched periodically in each clock cycle; the amount of data stored is constant and the amount of data fetched necessarily is even with adder and multiplier data flow i.e. one data word regardless of its particular bit length. The IIR filter consists of series of 2nd Order Sections. The internal 2nd Order Sections (not the first, not the last in the series) need to store five times less amount of data than read – one storage per five fetches and accumulate cycles. The first SOS input data and the last SOS output data have to be stored somewhere too, but we neglect it for now. Instead of using discrete D-type flip-flop in FPGA fabric it is more efficient to use addressable memory because the amount of data stored and fetched in each clock cycle is small (up to one word). Considering Spartan-6 FPGA there are two possibilities of addressable memory. The first is distributed memory (special mode of Configurable Logic Blocks configuration memory) with 64x1 bit granularity which can be used for filters with sample rates from ones to tens Msps or equivalently ones MSOSps at design frequency 100 MHz. The other is block RAM (BRAM) with the capacity of 18 kbit each and configurable organization of port width from 1 to 36 bits.

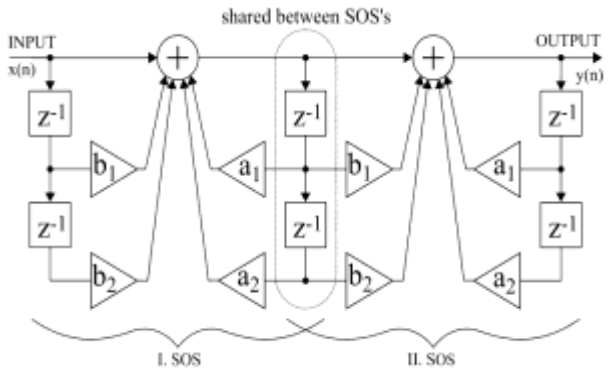

Fig. 3. Resource sharing between SOS's.

Considering the ideal fill, one BRAM can support up to 168 SOS's (in this extreme case, it is necessary to implement arithmetic in modulus 3 which is not particularly efficient for the FPGA implementation and all SOS's share the memory places with exception of the first one and the last one) what implies sample frequency in hundreds ksps.

With appropriate controller, this concept does not restrict implementation to just one filter but allows compute different filters for possibly different channels in one SOS cell based on one RAM, one multiplier and one adder, see Fig. 4. In a straightforward way, the sampling is simultaneous on all inputs so data comes synchronously but the controller can cover cases with different but commensurable sample rates or even with incommensurable sample rates.

TABLE I.
SOS CORE THROUGHPUT AND RESOURCE UTILIZATION

	Spartan-6 at 100 MHz
1 multiplier and 1 adder	12.5 to 20 MSOSps
distributed memory	suitable up to 10 SOS / sample
BRAM 512×36[1]	suitable up to 64 to 168 SOS / sample
BRAM 1024×18[2]	suitable up to 128 to 339 SOS / sample

III. CONTROLLER MICROCODE IMPLEMENTATION

Controller can be designed and implemented with common FSM design techniques (VHDL for example) but this way is complicated and gives unsatisfactory results in FPGA timing and space occupation; future modifications are complicated. As a more efficient way, the controller can be designed utilizing a program counter and RAM (BRAM in case of Spartan-6). A simple assembler language is suitable for writing controller microcode.

Table 2 displays example of computation two SOS's for one signal channel. The first section z-domain transfer function $H(z)$ is:

$$H(z) = \frac{\mathrm{Y(z)}}{\mathrm{X(z)}} = \frac{1-\frac{11}{8}z^{-1}+z^{-2}}{1-\frac{13}{8}z^{-1}+\frac{7}{8}z^{-2}} \quad (1)$$

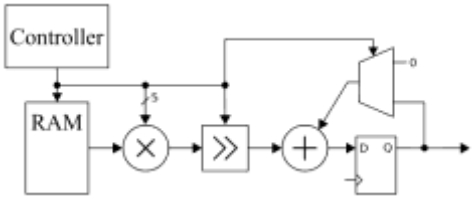

Fig. 4. SOS cell with programmable controller.

[1] Suitable for up to fixed-point int36 or single precision floating-point
[2] Suitable for up to fixed-point int18 or half precision floating-point

TELEN2019008
DOI 10.14311/TEE.2019.2.022

The second section z-domain transfer function $H(z)$ is:

$$H(z) = \frac{\mathrm{Y(z)}}{\mathrm{X(z)}} = \frac{1-\frac{5}{4}z^{-1}+z^{-2}}{1-\frac{5}{4}z^{-1}+\frac{1}{2}z^{-2}} \qquad (2)$$

TABLE II.
AN EXAMPLE OF CONTROLLER MICROCODE
IN SIMPLE ASSEMBLER LANGUAGE

```
input&store port(0), ram(0.0)
load ram(0.0), c=1/1
acc ram(0.2), c=−11/8
acc ram(0.1), c=1/1
acc ram(1.2), c=13/8
acc&store ram(1.1), c=−7/8, ram(1.0)
load ram(1.0), c=1/1
acc ram(1.2), c=-5/4
acc ram(1.1), c=1/1
acc ram(2.2), c=5/4
acc&store&output ram(2.1), c=−1/2, ram(2.0), port(0)
next3
```

IV. FILTER DESIGN AND OPTIMIZATION WORKFLOW

A. Allowed Poles and Zeros Locations

The most important part of the design of particular IIR filter is coefficient set. The width of multipliers increases demands for resources so the design aim is to minimize coefficient mantissa widths. The goal of the method of rounded coefficients is to obtain such coefficients that lead to multiplication and division by small integer numbers. Coefficient optimization is crucial otherwise unpredictable results can occur.

Fig. 5 displays possible pole locations for constants a_1, a_2 obtained as $n/8$ where n is integer. Because poles are complex conjugate, always symmetrical, the picture includes only the upper half of the complex plane.

For complex conjugate poles $p_{1,2} = c \pm d\mathrm{i}$ (and the same for zeros $n_{1,2}$) holds:

$$(z - p_1)(z - p_2) = z + a_1 z^{-1} + a_2 z^{-2}, \qquad (3)$$

where $a_1 = -2c = -2\Re(p_{1,2})$ and $a_2 = c^2 + d^2 = |p_{1,2}|^2$.

Because of these properties, allowed pole locations are grouped in columns with the same real part and in concentric circles with the same magnitude.

B. Poles and Zeros Location Optimization

For given filter poles and zeroes can be obtained using MATLAB with the command

```
[z,p,k]=cheby2(4,20,3/10);
```

Table 3 contains obtained and rounded coefficients and poles and zeros locations.

Fig. 6 displays the results of the original given filter and filter with rounded coefficients. According to the figure, the filter has too high attenuation in the region between 1/10 to 2/10 π·rad/sample.

Other parameters of the filter meet expectations. The attenuation in mentioned region is dominated by pole pairs $p_{1,2}$ from Table 3.

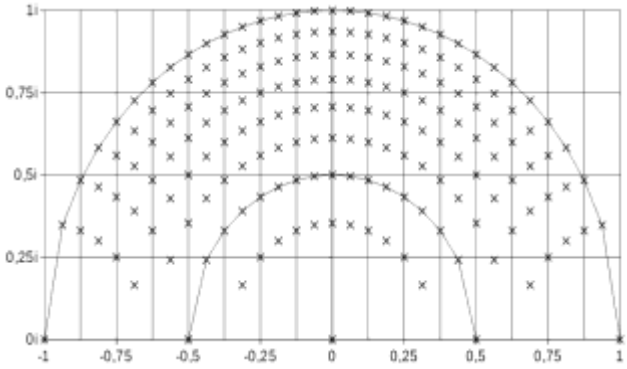

Fig. 5. Pole locations for constants $n/8$.

TABLE III.
POLES AND ZEROS LOCATIONS

	exact location	$n/8$ coefficients	rounded locations
		first iteration of rounding	
$p_{1,2}$	$0.3023 \pm 0.2725\mathrm{i}$	$a_1 = -5/8$; $a_2 = 1/8$	$0.3125 \pm 0.1654\mathrm{i}$
$z_{1,2}$	$-0.2787 \pm 0.9604\mathrm{i}$	$b_1 = 4/8$; $b_2 = 1$	$-0.25 \pm 0.9682\mathrm{i}$
$p_{3,4}$	$0.6015 \pm 0.5783\mathrm{i}$	$a_1 = -9/8$; $a_2 = 6/8$	$0.5625 \pm 0.6585\mathrm{i}$
$z_{3,4}$	$0.5336 \pm 0.8458\mathrm{i}$	$b_1 = -1$; $b_2 = 1$	$0.5 \pm 0.866\mathrm{i}$

TABLE IV.
POLE PAIR $P_{1,2}$ RELOCATION

	p	$\lvert p\rvert^2 = a_2$	arg p
original $p_{1,2}$	$0.3023 \pm 0.2725\mathrm{i}$	0.1656	±0.7337
relocated $p_{1,2}$	$0.3125 \pm 0.1654\mathrm{i}$	0.125	±0.4868

Poles cause peaks in the magnitude transfer characteristics of a filter. An argument (arg p) determines the frequency of a peak whereas an absolute value (abs p) determines the magnitude of the peak.

Rounding quoted in Table 4 moves the pole pair $p_{1,2}$ towards lower frequency and lower magnitude.

Fig. 7 displays other five possible relocations of the pole pair $p_{1,2}$ using constants n/8. Better results can be obtained with a pole pair with different absolute value and argument combination.

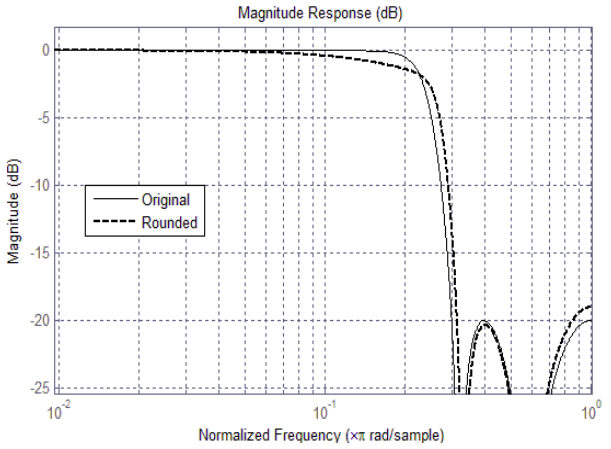

Fig. 6. Influence of coefficients rounding on filter.

TELEN2019008
DOI 10.14311/TEE.2019.2.022

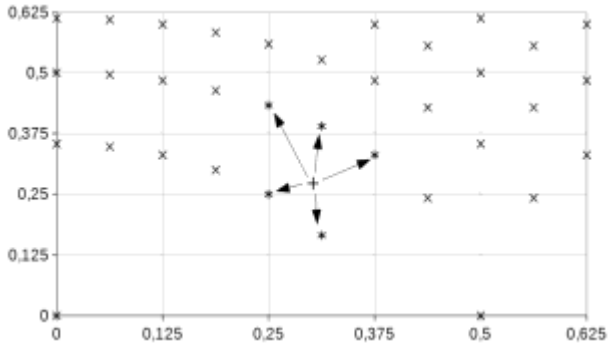

Fig. 7. Other possible pole pair $p_{1,2}$ relocations.

Fig. 8 shows frequency response of the original filter and two other filters with alternative pole pairs $p_{1,2}$ locations. The most suitable results yield the pole [1 –6/8 2/8].

In the matter of zeros, it is interesting to note that many IIR filter design methods place zeros on the complex unit circle ($b_2 = 1$), the only remaining parameter is then b_1. The smallest resolution occurs for filters with very low or very high[3] cutting frequencies. Therefore the method of rounded coefficients is not sufficient for filters with cut off frequency too much low or too much high in comparison to sample frequency. In the case of low frequencies, there might help to decimate the signal first or process the signal via a filter with the finite response (FIR), moving average filter or sinc^k filter can be a good candidate.

Implementation of the filter which operates on the decimated signal causes the poles and zeros are moved to higher values of arg *p*. Moreover, filter with poles close to the complex unity circle has higher demands for accumulation accuracy.

C. Overall Filter Gain

Every 2nd Order Section has its DC gain *g*:

$$g = \frac{b_0+b_1+b_2}{a_0+a_1+a_2} \tag{4}$$

Implementation of IIR filter with accumulator and microcode requires that $a_0 = 1$. Because b_0 is a parameter that can be chosen, the overall gain of all 2nd Order Section (whole filter) can be set to match the final filter realization. For example, the gain of all sections can be matched to 2^n so it is possible to divide the output of the filter just by shifting right.

Resolution of placement of zeros on the complex unit circle can be improved by replacing coefficient $b_0 = b_2$ to some other value than 1.

Regarding the fact that b_1/b_0 ratio need not be only $n/2^k$ but can reach other values n/k (for example 5/7, 6/7, 8/9) zero pairs can be selected from a finer set on complex unity circle.

[3] Near Nyquist frequency (sample frequency / 2)

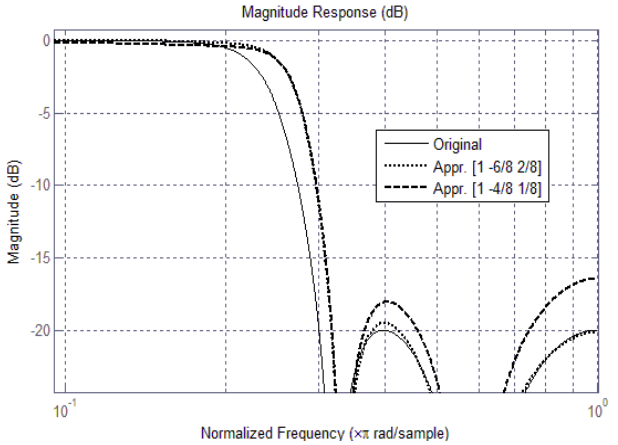

Fig. 8. Influence of relocation of the pole pair $p_{1,2}$.

D. Risk of Arithmetical Overflow

If it is guaranteed that the output of 2nd Order Section accumulator does not overflow (after the last accumulation has been done), there is no need to check overflow during the accumulation process assuming the accumulator uses two's complement representation. The maximal overshoot for each 2nd Order Section should be determined by simulation using step response. For the best results, SOS with the highest gain and the lowest overshoot should be placed first in series of SOS for reaching smaller rounding error (gain) and more arithmetical resources used by valid signal (overshoot).

V. Conclusion

Modern mid-range FPGAs can process IIR filters on very high throughput. IIR filter need not be designed with floating point arithmetic and with full fixed-point or floating-point multipliers. For a great number of filters with cutting frequencies in a reasonable ratio to the sampling frequency, the poles and zeros locations can be optimized so that IIR filter coefficients are round numbers whose multiplication can be realized without a complex multiplier. Utilizing the microcode controller and creating time multiplex allow recycling the FPGA fabric of IIR 2nd Order Section cell in a highly effective way for filtering more signals with different filter coefficients.

References

[1] R. Landry, V. Calmettes and E. Robin, “High speed IIR filter for XILINX FPGA,” in *1998 Midwest Symposium on Circuits and Systems (Cat. No. 98CB36268)*, Notre Dame, IN, 1998, pp.46-49.

[2] S. T. Pan, “Evolutionary Computation on Programmable Robust IIR Filter Pole-Placement Design,” *IEEE Transactions on Instrumentation and Measurement*, vol. 60, no.4, pp.1469-1479, April 2011. https://doi.org/10.1109/TIM.2010.2086850

[3] R. G. Lyons, “Infinite impulse response filters,” in *Understanding digital signal processing*, 2nd ed., New Jersey, USA: Pearson Education Inc. 2008, ch. 6, pp. 211–282.

[4] U. Meyer-Baese, “Infinite impulse response (IIR) digital filters,” in *Digital signal processing with Field Programmable Gate Arrays*, 4th ed., Heidelberg, Germany: Springer-Verlag Berlin Heidelberg. 2014, ch. 4, pp. 225–304. https://doi.org/10.1007/978-3-642-45309-0_4

Summary of the Modern Wheel Slip Controller Principles

Petr Pichlík [1)]

[1)] CTU in Prague, FEE, Department of Electric Drives and Traction, Prague, Czech Republic, e-mail: *pichlpet@fel.cvut.cz*

Abstract — **Railway traction vehicles need to transfer high tractive effort from wheels to rails. The task is complicated because the maximum transferable force continuously changes during the train run, and the change can lead to the high wheels slip velocity or slippage. The effects are undesirable and must be prevented if it is possible or at least limited by slip controllers. There have been several slip controllers developed based on different principles with different degree of complexity and efficiency. The paper summarises principles of the slip control methods and brings their overview with the simulation of their behaviour**.

Keywords — adhesion, railway, traction, wheel slip control.

I. Introduction

The modern railway vehicles can transport a large number of cargo or passengers to long distance. To be possible to reach the high tractive effort that is required by cargo trains or high speed required by passengers trains the force from wheels to rails have to be transferred effectively. The requirement is obvious, but due to the steel contact areas between wheels and rails, it can be challenging to fulfil it, especially during bad weather because the force that can be transmitted between wheels and rails depends on the adhesion that is closely linked with the rails surface conditions thus with the weather. The locomotives are designed to fully utilise all available adhesion during good conditions when the adhesion coefficient has a high value. However, when the conditions become worse, the locomotive can produce higher tractive force than the force that can be transferred by the wheel-rail contact. If the force is not limited, the slippage of the wheels is the result in the case. The slippage is undesirable because it increases wear of wheels and rails [1] and can damage mechanical parts of the locomotive bogie in the worst cases. Once slippage is created, it must be suppressed by the massive tractive force decrease. If the force is decreased many times, the train can gain delay [2] or even suck at the track. The problem was solved by the gradual development of many types of slip controllers. The early controllers were protections that eliminate the slippage if it occurs. The modern ones can prevent slippage occurrence by early regulatory intervention. The problem with the force transfer have all railway vehicles not only locomotives. However, other railway traction vehicles like multiple units have a higher number of driven wheelsets and reach lower force. Therefore, their maximum force requires lower adhesion, and the slippage occurs when the rails surface conditions are very adverse.

The slip controllers for railway traction vehicles are developed for many decades, and their development still continues. The new or improved slip controllers are developed because the slip control problem is not sufficiently solved. The slip controller basic purpose is to enable the maximum force transfer by the wheel-rails contact area if the required force is higher than the maximum transferable force due to an adhesion limitation. The slip controller must also keep the slip velocity, i.e. difference between wheel circumference velocity and its longitudinal velocity, at an acceptable value to limit wear of wheels and rails. Therefore, the slip controller has to change the required tractive force to fulfil the requirements continuously. Moreover, to the modern slip controllers are put new demands like suspension of torsional vibrations that occur in the wheelset mechanical system, and the torsional vibrations amplitude is connected with the adhesion. Although the slip controllers are developed for decades, their summary is missing, or it is incomplete. Therefore, the paper summarises the most common slip controller principles and describes modern and perspective slip controllers in more detail.

The rest of the paper is organised as follows. The adhesion phenomenon and its influence to the tractive force transfer by the wheel-rail contact are described in the next chapter because the adhesion is essential for the slip controller operation and design. The slip controllers overview and detailed description of the most used is described next. Finally, the simulation of the selected slip controllers is described.

II. Adhesion and Forces

The adhesion is crucial for the tangential force transfer between wheels and rails during traction or braking. Therefore the description of the slip controllers is preceded the description of the adhesion. The tangential force can be expressed as follows.

$$F_{\mathrm{T}} = \mu \cdot W \cdot g \tag{1}$$

Where F_{T} is a tangential force, μ is an adhesion coefficient, W is an adhesion weight, and g is the gravity acceleration.

The value of the adhesion coefficient depends on many parameters like wheel slip velocity, train longitudinal velocity and conditions on rails surface. The slip velocity is a difference between the wheel circumference velocity and its longitudinal velocity. The circumference velocity can be measured by incremental encoders mounted on wheels or motor. However, to determine the longitudinal velocity is difficult when all wheels are driven, and the velocity has to be calculated by some averaging or has to be estimated in this case. The slip velocity is necessary for the tangential force transmission between the wheel and the rail. Therefore, every driven or braked wheel has to

TELEN2019009
DOI 10.14311/TEE.2019.2.026

have different circumference velocity from its longitudinal velocity, thus slip velocity [3]. Examples of the dependence of the adhesion coefficient on the slip velocity for different adhesion conditions are depicted in Fig. 1 and wheel with depicted forces and velocities are depicted in Fig. 2. The adhesion characteristic can be divided into the two areas from the electric drive control point of view. The first area of the characteristic is called a stable area, and the area is from zero value of the slip velocity to approximately 2 $km \cdot h^{-1}$ [4]. The area is called stable because the slip controller can work in the area without any controller reaction. An unstable area is located behind the stable area. Between the areas is located the maximum point of the characteristic. The maximum point moves to higher slip velocities and lowers adhesion coefficient values when the rail surface conditions are getting worse. The goal of the slip controller is to keep the slip velocity in the stable area in passenger trains or multiple units case and the stable area or not far from the peak value in the unstable area in freight trains [5].

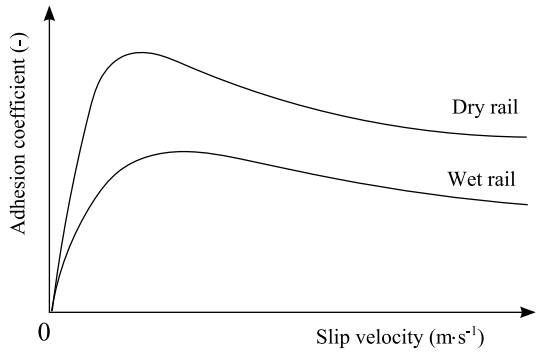

Fig. 1 Example of the adhesion characteristics for different rail surface conditions

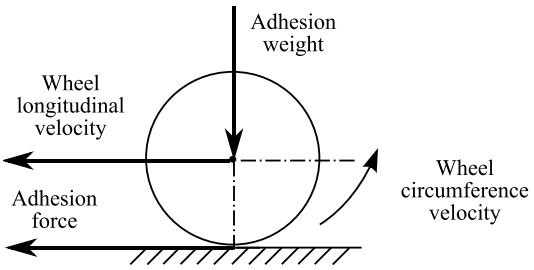

Fig. 2 Wheel and applied forces and velocities

From the previous description, it is clear that the slip velocity affects the value of the actual adhesion coefficient from zero to the maximum value. However, the conditions of the rail surface, train velocity and temperature affect the maximum value of the adhesion coefficient and position of the maximum point on the adhesion characteristic. The influence of the rail surface conditions are random and cannot be predicted. The adhesion coefficient can reach values from 0.05 to 0.4 due to the rail surface changes [6]. Moreover, the adhesion changes approximately every few meters even when the wheatear is unchangeable. On the other hand, the effect of the velocity is described by well-known Curtius and Kniffler formula [6]. The maximum value of the adhesion coefficient decreased with increased velocity according to the formula.

The second parameter from (1) that affects the value of the tangential force is the adhesion weight. The value of the adhesion weight changes when the dynamic motions of the locomotive occur e.g. pitches or bounces. These phenomena are related to the locomotive mechanical parameters, values of the tractive effort, load, changes of the tractive effort and track parameters.

III. Slip Controllers

The slip control methods can be sorted into several groups according to their principle of operation [7] or target railway vehicle [5], but not exactly given slip control methods classification is presented in the literature. Generally, the slip control methods can be sorted into a forerunner of the modern slip controllers to the re-adhesion controllers and the slip controllers with different level of regulation quality and principles [8]. Proposed slip control methods classification that takes into account the methods evolutionary and principle of the operation is depicted in Fig. 3. Some of the methods from the picture are also described in [9] in detail.

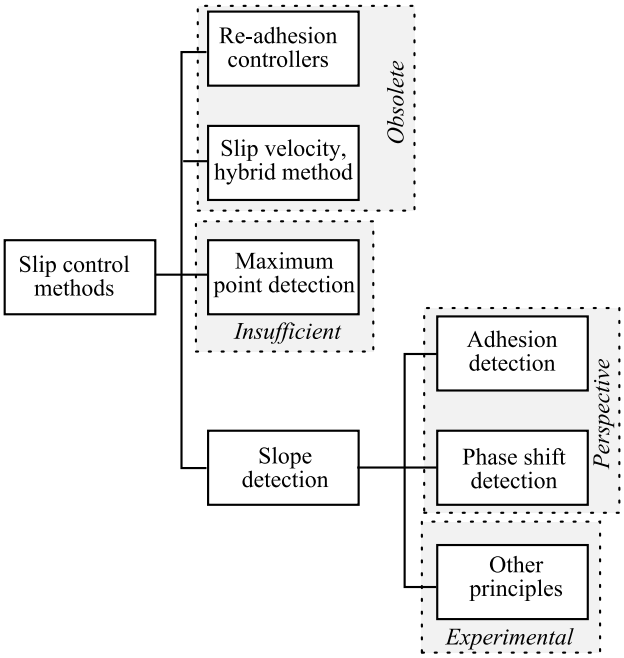

Fig. 3 Proposed slip control methods sortation

The first of the slip control methods were re-adhesion controllers. The re-adhesion controllers work as a protection against the slippage when it occurs. They are typically based on the slip velocity comparison with a fixed predefined threshold. If the threshold is overstepped, the controller steeply decreases the tractive force. Another re-adhesion controller is based on the wheel acceleration comparison with a predefined threshold. These methods can simply fail due to slow slippage creation or by slippage of all wheelset. Another principle is based on the voltage or current difference between serially or in parallel connected motors. If the difference occurs, one wheelset is in slippage. The re-adhesion controllers cannot prevent the slippage creation and can only limit it. The re-adhesion controllers steeply decrease the tractive force when the slippage is detected, and after slippage suppression, it starts the force increase to the initial level. This behaviour often leads to another slippage creation, and the locomotive driver must decrease the required tractive force to prevent another slippage creation.

TELEN2019009
DOI 10.14311/TEE.2019.2.026

From the re-adhesion controllers, the first slip controllers were developed. This slip controllers control the slip velocity to a constant value. The value of the required slip velocity is set as the higher acceptable value on which slippage does not occur. The slip controller main disadvantage is low adhesion utilisation, and the slip velocity calculation is also problematic. The slip controller is often improved about acceleration protection to create a hybrid slip controller [10]. These slip controllers can be used as additional protection to the modern slip controllers to work as protection when they potentially fail.

The modern slip controllers try to avoid slippage formation by preventive and continuous regulatory interventions. The modern slip controllers are based on the determination of the actual adhesion characteristic parameters. The determined parameters can be the maximum point location on the actual adhesion characteristic or slope of the actual characteristic. Moreover, the slip controller can be sorted according to the adhesion or slip detection mechanism. The slip controllers based on the slope determination requires knowledge of the adhesion parameters like adhesion coefficient or adhesion force. However, none of these parameters can be directly measured during train runs. Therefore, the slip controllers use estimation techniques to determine the value. The estimators can be disturbance observer [11] or some variant of the Kalman filter [12]. The different way how to determine the slope is based on a mechanical phenomenon that occurs in the torque transfer chain between electric motor and wheels, i.e. determination of a phase shift between motor torque and its velocity [13] or according to torsional vibrations [14].

Slip controllers that detect a maximum point position [15] can fully utilise the whole available adhesion, but they must permanently work in the unstable area of the adhesion characteristic. Therefore, the slip controllers require a highly dynamic electric drive. The main disadvantage of the slip controllers based on the principle is that they can cause some undesirable mechanical effects that are connected with stick-slip oscillations that occur when the operating point moves from the stable area to the unstable area and back [16].

There are also exists other slip controllers based on different principles described in the literature. Methods that evaluate noise [17], or use a Hilbert-Huang transformation [18]. However, the approaches are experimental.

The explanation of the main difference between the selected principles of the slip controllers is depicted in Fig. 4. The figure shows a set of adhesion characteristics for different conditions of the surface of the rails and the positions of the operating points for different slip controllers principles when the maximum force has to be transferred. The simple slip controller control slip velocity to a constant can optimally work with the good adhesion characteristic. On the other hand, the modern slip controllers can work near the maximum point with good adhesion characteristic. However, the slip controller based on the adhesion characteristic slope detection as the only one can work with acceptable slip velocity value when the adhesion is adverse because the method that controls to the maximum point moves the operating point to unacceptable higher slip velocities when the adhesion is adverse.

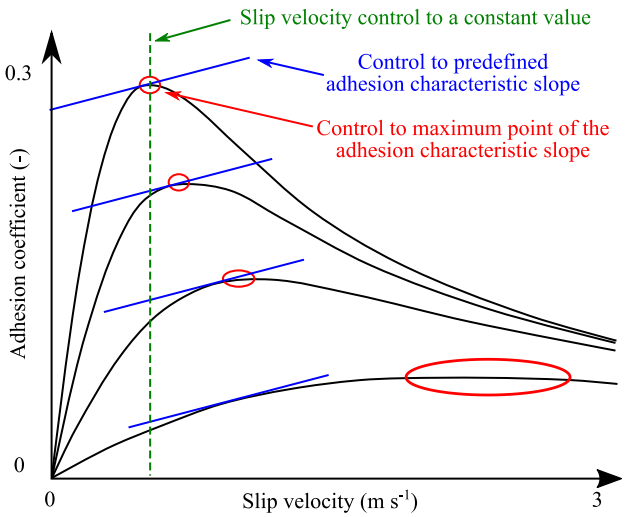

Fig. 4 Slip controllers principles comparison

A. Adhesion Characteristic Slope Determination

Because the slip controllers that estimates the adhesion characteristic slope is perspective, the principles of the slip controller are described in more detail in the subchapter. This group of methods is based on two different approaches. The first approach uses the adhesion estimation by a proper estimator according to slip velocity and applied force change. The second approach estimates adhesion according to the phase shift between motor angular velocity and wheel angular velocity.

The slip controllers that estimates the adhesion characteristic slope according to adhesion estimation typically estimates the adhesion coefficient or force adhesion force and calculate a derivative of the adhesion force F_A and the slip velocity v_s. The derivative can be calculated as follows:

$$\frac{\mathrm{d}F_A}{\mathrm{d}v_S} = 0 \tag{2}$$

When (2) is met, the operating point is located in the maximum point of the adhesion characteristic. If the derivative is positive, the operating point is located in the stable area of the characteristic, and if the derivative is negative, the operating point is located in the unstable area of the characteristic. The slip controller can basically detect the maximum point of the adhesion characteristic. However, the controller structure has to be highly dynamic, and the usage of the speed controller is recommended. However, the speed controller is not a standard part of the locomotive control structure, and it would have to be installed.

The possible estimators can be disturbance observers or the proper variant of the Kalman filter. The typically used disturbance observers are zero order, first order or full order. The difference between the observer orders lays in its complexity and accuracy. The simple disturbance observers can sometimes have problems with proper function [19]. More accurate results can be achieved by using a Kalman filter, extended Kalman filter or unscented Kalman filter [20]. The adhesion coefficient can also be estimated according to a wheel-rail contact area [21]. The slip controllers are based on a model of the contact area,

TELEN2019009
DOI 10.14311/TEE.2019.2.026

and an adaptive sliding mode controller is used for the control. However, the method was not verified.

The general description of the slip controllers group is depicted in Fig. 5. The slip controller input is a required torque that is set by a train driver. The required torque is multiplied by a slip controller output value that is in a range from zero to one. Therefore, the slip controller can only limit the value. The decreased required torque is led to a torque controller block, and then to an electric drive block. The electric drive block output is measured motor or wheel velocity v and calculated motor torque. The motor torque is calculated by a motor controller. The torque and the velocity are led to the estimator block that estimates force. Then, a derivative is calculated. If the Kalman filter is used, the derivative cannot be calculated because the slope is the output of the Kalman filter. The PI controller output maintains the required torque value to be the PI controller input equal to zero or positive. The positive value is used more often to avoid the operating point oscillates around the maximum point. When the PI controller input is maintained at a positive value, the operating point is located in the stable area of the adhesion characteristic.

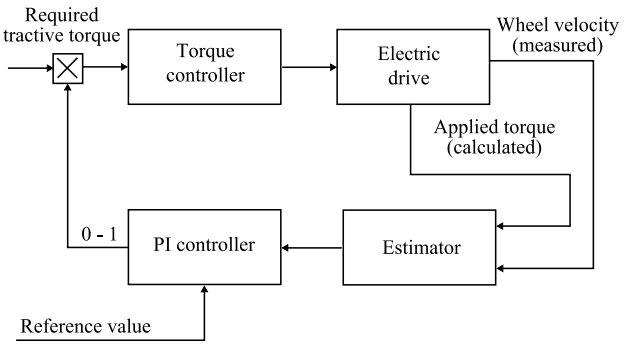

Fig. 5 General principle of the slip controller that estimates adhesion characteristic slope by estimator

The second approach is based on the measuring of the phase shift between the signal injected to the electric motor torque and its representation measured on wheel or motor angular velocity. The slip controller was initially presented in papers [13] and [22]. The slip controller requires adding a small periodic excitation torque signal to the required motor torque. The excitation torque causes oscillations of the motor torque and correspondingly angular speed. Between the motor torque oscillations and motor angular speed, a phase shift occurs. The phase shift is proportional to the actual adhesion characteristic slope. The principle of the slip controller is simple. The wheelset with electric drive creates a mechanical system with eigenfrequencies, and its poles are located in a stable position. However, the adhesion brings to the system additional damping that depends on the operating point position on the adhesion characteristic [23]. The additional damping changes the mechanical system parameters and causes the phase shift. The slip controller principle is described in [9].

The method general block diagram is depicted in Fig. 6. The block contains a generator of the excitation signal that is led to the electric drive. Basically, the signal can be added to the required torque in any part of the diagram. The applied torque and measured velocity are led to the angle calculation block diagram, and its output is led to the controller.

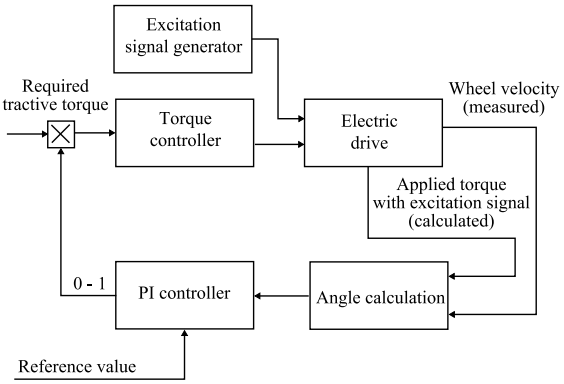

Fig. 6 General principle of the slip controller that estimates adhesion characteristic slope phase shift between torque and velocity

IV. Simulation Results

Simulation results for selected slip controllers for dry and wet rails are depicted in Fig. 7 and Fig. 8 respectively. The upper part of the figures depicts forces, and bottom part depicts velocities. The adhesion force is used as a basement that represents the highest possible achievable adhesion. The applied tractive forces have to be below the adhesion force to avoid slippage creation and the distance from the adhesion force is expresses regulatory quality of the slip controller. The adhesion force decreases at time 3 second and then starts to increase to the original value. The slip controller reaction in this part is crucial for comparison of the slip controller reaction. The figures compare the slip controller that estimates the slope of the adhesion characteristic with the method that keeps the slip velocity at the constant value. The slip controllers that determine the slope of the adhesion characteristic is based on the Kalman filter (marked as KF in the legend), disturbance observer (marked as DO) and phase shift (marked as phase).

Simulation results for dry rails are depicted in Fig. 7. All tractive forces are below the adhesion force. The highest tractive force and thus, the highest adhesion utilisation have the slip controller based on the phase shift determination and slip controller that control slip velocity to the constant value. However, the slip controller that determines the phase shift has the highest slip velocity that increases the wear of the wheels and rails. Although the slip controller has the best results, the controller should be set to have a lower slip velocity, and the results would be similar to the slip controller based on the Kalman filter. Note that there is a visible excitation signal on the torque and velocity of the slip controller that determines the slope of the adhesion characteristic from the phase shift.

Simulation results for wet rails are depicted in Fig. 8. The best results in the case produce the slip controller based on the Kalman filter because it has the highest average force with low slip velocity. The slip controller that controls the slip velocity has the worst results because the maximum point of the adhesion characteristic is located at higher slip velocity, and the slip controller cannot utilise the available adhesion.

TELEN2019009
DOI 10.14311/TEE.2019.2.026

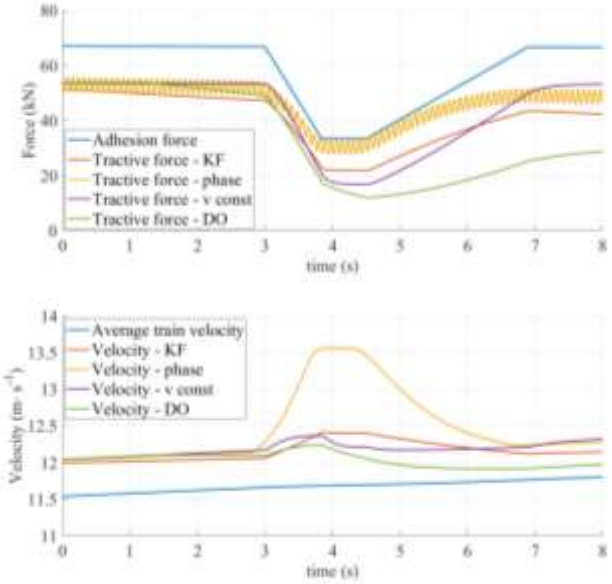

Fig. 7 Simulation results of selected slip controllers for dry rails

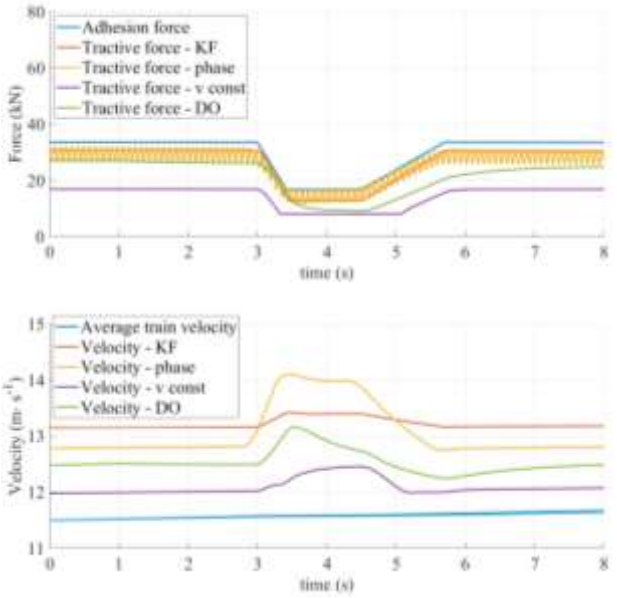

Fig. 8 Simulation results of selected slip controllers for wet rails

V. Conclusions

The slip controllers are a crucial part of railways traction vehicles because they enable to reach high tractive effort and speed during all conditions. Moreover, the slip controllers increase the economy of operation by decreasing wear of wheels and rails and can avoid train delay. The paper summarises developed approaches to slip control. The slip controllers were gradually developed from simple methods that were only protection or control the slip velocity to the constant value to the modern slip controllers based on complicated algorithms. The slip control is inseparable from the adhesion. Therefore, the paper starts with the description of the adhesion and its relation to wheel slip. Then, the existing slip controllers are sorted into groups. The methods based on the detection of the slope of the adhesion slip characteristic. However, from the simulation results, it is clear that the estimation has to be made by a stochastic filter, e.g. Kalman filter or method that must change complete locomotive control.

Acknowledgment

This work was supported by the Technology Agency of the Czech Republic under the grant No. TE02000103, Center for Intelligent Drives and Advanced Machine Control.

References

[1] I. Hussain, T. X. Mei, and R. T. Ritchings, "Estimation of wheel–rail contact conditions and adhesion using the multiple model approach", *Vehicle System Dynamics*, vol. 51, no. 1, pp. 32–53, Jan. 2013. Doi: https://doi.org/10.1080/00423114.2012.708759

[2] X. Cao *et al.*, "The effect of alumina particle on improving adhesion and wear damage of wheel/rail under wet conditions", *Wear*, vol. 348–349, pp. 98–115, Feb. 2016. Doi: 10.1016/j.wear.2015.12.004

[3] R. I. Popovici "Adhesive in Wheel - Rail Contacts," Ph.D. dissertation, Univ. of Twente, Enschede, The Netherlands, 2010.

[4] T. Watanabe, "Anti-slip Readhesion Control with Presumed Adhesion Force. Method of Presuming Adhesion Force and Running Test Results of High Speed Shinkansen Train," Quarterly Report of Railway Technical Research Institute, QR of RTRI, vol. 41, No. 1, Mar 2000. Doi: https://doi.org/10.2219/rtriqr.41.32

[5] K. Kondo, "Anti-slip Control Technologies for the Railway Vehicle Traction". 2012 IEEE Vehicle Power and Propulsion Conference, Seoul, Korea, 2012, pp. 1306-1311. Doi: 10.1109/VPPC.2012.6422493

[6] *Wheel-rail interface handbook*, 1 st Ed., CRC Press, Cambridge, 2009.

[7] L. Diao, L. Zhao, Z. Jin, L. Wang and S. M. Sharkh, "Taking Traction Control to Task: High-Adhesion-Point Tracking Based on a Disturbance Observer in Railway Vehicles," in *IEEE Industrial Electronics Magazine*, vol. 11, no. 1, pp. 51-62, March 2017. Doi: 10.1109/MIE.2016.2644699

[8] K. Xu, G. Xu, and C. Zheng, "Novel determination of Wheel-Rail adhesion stability for electric locomotives", *Int. J. Precis. Eng. Manuf.*, vol. 16, no. 4, pp. 653–660, Apr. 2015. Doi: https://doi.org/10.1007/s12541-015-0087-0

[9] P. Pichlik and J. Zdenek, "Overview of slip control methods used in locomotives", *Transaction on Electrical Engineering*, Vol.3, No.2, 2014.

[10] J.n Huang, J. Xiao and H. Weiss, "Simulation study on adhesion control of electric locomotives based on multidisciplinary virtual prototyping," *2008 IEEE International Conference on Industrial Technology*, Chengdu, 2008, pp. 1-4. Doi: 10.1109/ICIT.2008.4608616

[11] W. Lin, Z. Liu, L. Diao, G. Zhang, D. Chen and Z. Li, "Maximum Adhesion Force Control Simulated Model of Electric Locomotive," *2007 IEEE International Conference on Automation and Logistics*, Jinan, 2007, pp. 1704-1708. Doi: 10.1109/ICAL.2007.4338847

[12] S. Wang, J. Xiao, J. Huang, and H. Sheng, "Locomotive wheel slip detection based on multi-rate state identification of motor load torque, " *Journal of the Franklin Institute*, vol. 353, no. 2, 2016, pp. 521–540. Doi: https://doi.org/10.1016/j.jfranklin.2015.11.012

[13] R. Schreiber and P. Kögel "Identifikationsmethode zur Bestimmung der Adhäsion zwischen Rad und Schiene," (in German), *ZEV GA*. vol. 120, no. 2, p. 48-54, 1996.

[14] T. X. Mei and I. Hussain, "Detection of wheel-rail conditions for improved traction control," *IET Conference on Railway Traction Systems (RTS 2010)*, Birmingham, 2010, pp. 1-6. Doi: 10.1049/ic.2010.0036

[15] M. Buscher, R. Pfeiffer and H. J. Schwartz, "Radschlupfregelung für Drehstromlokomotiven," (in German), *EB*. vol. 91, no. 5, p. 163-178 1993

[16] R. Stock, L. Stanlake, C. Hardwick, M. Yu, D. Eadie, R. Lewis, "Material concepts for top of rail friction management – Classification, characterisation and application" Wear, vol. 366-367, 2016, pp. 225-232. Doi: https://doi.org/10.1016/j.wear.2016.05.028

[17] M. Spiryagin, K. S. Lee and H. H. Yoo, "Control system for maximum use of adhesive forces of a railway vehicle in a tractive mode“, *Mechanical Systems and Signal Processing*, vol. 22, no. 3, 2008, pp. 709-720.
Doi: https://doi.org/10.1016/j.ymssp.2007.09.018

[18] J. Huang, J. Xiao, D. Zhao and S. Wang, "A wheel slip detection method of electric locomotive based on time-frequency analysis," *17th International IEEE Conference on Intelligent Transportation Systems (ITSC)*, Qingdao, 2014, pp. 1221-1225.
Doi: 10.1109/ITSC.2014.6957854

[19] K. Ohishi, Y. Ogawa, I. Miyashita and S. Yasukawa, "Anti-slip re-adhesion control of electric motor coach based on force control using disturbance observer," *Conference Record of the 2000 IEEE Industry Applications Conference. Thirty-Fifth IAS Annual Meeting and World Conference on Industrial Applications of Electrical Energy (Cat. No.00CH37129)*, Rome, 2000, pp. 1001-1007 vol.2.
Doi: 10.1109/IAS.2000.881954

[20] P. Pichlík. "Comparison of Different Kalman Filters Types Performance for a Locomotive Slip Control Purposes" Poster 2017. Prague: CTU in Prague, 2017

[21] S. H. Park, J. Kim, J. J.Choi and H. Yamazaki, "Modeling and control of adhesion force in railway rolling stocks," *Control Systems, IEEE* , vol.28, no.5, pp.44-58, October 2008.
Doi: 10.1109/MCS.2008.927334

[22] R. Schreiber, P. Kögel, P. Häse, and P. Hildenbrand, "Regelung zur optimalen Kraftschlußausnutzung bei Drehstromlokomotiven auf der Basis der Steigung der Kraftschlußkennlinie," (in German), *EB*, vol. 93, no. 5, p. 157-173, 1995

[23] J. Liu, H. Zhao, and W. Zhai, ‘Mechanism of self-excited torsional vibration of locomotive driving system’, *Front. Mech. Eng. China*, vol. 5, no. 4, pp. 465–469, Dec. 2010.
Doi: https://doi.org/10.1007/s11465-010-0115-9

TELEN2019009
DOI 10.14311/TEE.2019.2.026

Sivkov, O., Musalek, L., Novak, J., Novak, M., Chysky, J. and Novak. L.: **Development of Urban Electric Bus Drivetrain**

The development of the drivetrain for a new series of urban electric buses is presented in the paper. The traction and design properties of several drive variants are compared. The efficiency of the drive was tested using simulation calculations of the vehicle rides based on data from real bus lines in Prague. The results of the design work and simulation calculations are presented in the paper.

Zoubek, O., Musil, T.: **High Performance IIR Filter FPGA Implementation Utilizing SOS Microcode Core**

This paper discusses the methods of optimal IIR filter FPGA implementation. The methods are focused on the reduction of occupied resources and increasing data throughput. Higher demands on an internal controller complexity are successfully solved by utilizing programmable microcode controller. The novelty of SOS core and its capabilities are presented and different variants of SOS core are assessed. The workflow of IIR filter design using MATLAB considering rounded coefficient method is demonstrated.

Pichlík, P.: **Summary of the Modern Wheel Slip Controller Principles**

Railway traction vehicles need to transfer high tractive effort from wheels to rails. The task is complicated because the maximum transferable force continuously changes during the train run, and the change can lead to the high wheels slip velocity or slippage. The effects are undesirable and must be prevented if it is possible or at least limited by slip controllers. There have been several slip controllers developed based on different principles with different degree of complexity and efficiency. The paper summarises principles of the slip control methods and brings their overview with the simulation of their behaviour